Saddle-splay-induced periodic edge undulations in smectic-*A* disks immersed in a nematic medium

K. S. Krishnamurthy,[1,*] D. S. Shankar Rao,[1] Madhu B. Kanakala,[1]
Channabasaveshwar V. Yelamaggad,[1] and N. V. Madhusudana[2,*]
[1]*Centre for Nano and Soft Matter Sciences, P. O. Box 1329, Jalahalli, Bangalore 560013, India*
[2]*Raman Research Institute, Bangalore 560080, India*

(Received 19 December 2019; accepted 26 February 2020; published 17 March 2020)

We report experimental studies on the phase behavior of binary mixtures of 1″,7″-bis(4-cyanobiphenyl-4′-yl)heptane (CB7CB) and 4,4-diheptyloxyazoxybenzene, which exhibit, apart from the nematic (N) and twist-bend nematic (N_{TB}) phases, the induced smectic-A (Sm-A) phase for weight fraction of CB7CB between 0.05 and 0.70. In planar nematic layers, the N_{TB} phase separates as droplets of tactoidlike planform; the chirality of droplets manifests in the optical dissimilarity between their opposite angular ends. Our main result is that, in the appropriate two phase region, Sm-A nuclei with positive dielectric anisotropy change over to *disks* immersed in the nematic above some electric field, their edges decorated by *periodic bright spots*, a result which was earlier reported in another binary system exhibiting the induced Sm-A phase [R. Pratibha and N. V. Madhusudana, Physica A **224**, 9 (1996)]. We develop a simple theory for the *threshold* of this distortion, which is a periodic undulation of the edge of the disk, demonstrating that it arises from *saddle-splay elasticity* of Sm-A, the low Sm-A–N interfacial tension unable to suppress the distortion. The observed increases in the number of bright spots with field, and with the radius of the disk at a given field, in both the experimental systems are also accounted for by the model. The distortion, which results in the most direct visualization of saddle splay in Sm-A, is also exhibited by disks nucleating on surfaces treated for homeotropic anchoring.

DOI: 10.1103/PhysRevE.101.032704

I. INTRODUCTION

Smectic-A (Sm-A) liquid crystals (LCs) are characterized by a stacking of liquid layers made of freely rotating rodlike molecules, with the director **n** oriented along the layer normal direction [1]. In single component materials taken in cells with untreated glass plates, Sm-A nuclei separate from either the isotropic (I) or the nematic (N) phase as bâtonnets, the interfacial energy ($\sim r^2$, r being the drop size) dominating over curvature elastic energy ($\sim r$); the layer structure is mainly determined by the anisotropy of interfacial tension $\Delta\gamma = \gamma_{\parallel} - \gamma_{\perp}$, where $\gamma_{\perp}$ corresponding to the smectic layers orthogonal to the Sm-A–I (or N) interface is lower than $\gamma_{\parallel}$ corresponding to the layers parallel to it [2]. Well aligned monodomain Sm-A samples can be prepared in cells whose inner walls are treated for homeotropic anchoring, or by drawing the LC across mm-sized holes, with the free-standing films having 2–100s of layers [3]. After careful annealing, the central regions of the latter will have no defects, though a meniscus with a variable number of layers forms near the walls of the hole. As we will see below, the solid boundaries of the samples suppress manifestation of an *intrinsic* property of the liquid layers. For unraveling this, it is useful to get a freely suspended Sm-A monodomain, which is not in contact with any solid boundaries. A good strategy for achieving this is to have a system with a relatively wide Sm-A–N or Sm-A–I biphasic region. Binary mixtures of two nematogenic compounds, one of them with a strongly polar cyano (CN) end group and the other with a relatively weaker polar group often form charge transfer complexes that exhibit the Sm-A phase in a wide range of compositions, even if neither component by itself is a smectogen [4]. Such an induced Sm-A LC often coexists with either the N or I phase, over a range spanning several K.

In an early study of such a binary system made of rodlike molecules (pentylcyanoterphenyl and 4-biphenyl4"-n-decyloxybenzoate) [5], it is found that, as the sample is slowly cooled across the coexistence range, the induced Sm-A phase nucleates to form ellipsoidal droplets, with the geometry indicative of $\Delta\gamma$ being positive. Further cooling results in focal conic domains (FCDs) of type I [1], each with just a pair of conjugate elliptic and hyperbolic defects. The surrounding nematic liquid crystal, with *positive* dielectric anisotropy $\Delta\varepsilon$, reorients in a large enough applied AC field (E), with the director **n** ∥ **E**. The smectic drop itself *flattens out* to lower the dielectric energy, forming a disk with a number of layers. While the layer normal is parallel to **E** in the central region of the disk, it is distorted in the lateral periphery so that the disk is decorated with a *periodic pattern*, made of alternating dark and bright spots. At any given voltage U, the number of such spots is proportional to the diameter of the drop, i.e., the pattern period does not depend on the drop size. Further, as different smectic disks may have different thicknesses, the periodicity may also be assumed to be relatively insensitive to the number of layers in the disk. The number of spots increases with U, at first slowly, but at a constant rapid rate beyond some high voltage. The periodicity of the structure depends only on U, whether it is increased or decreased as a function of time.

*Authors to whom correspondence should be addressed: murthyksk@cens.res.in; nvmadhu@rri.res.in

In this paper, we report experimental studies on another binary system in which the aforesaid observations are reproduced. In the mixture with positive $\Delta\varepsilon$ exhibiting the induced Sm-*A* phase, the highly polar compound is CB7CB. This dimer of CB moieties is of bent shape due to the odd (seven here) number of carbon atoms in the linking methylene chain; it shows a transition from the *N* to N_{TB} phase, the latter made of pairs of the dimers arranged in double helical chains, with the twist director having an orientational order [6]. The weakly polar component is 4,4-diheptyloxyazoxybenzene (HOAB), showing the *N* and Sm-*C* phases. In the coexistence range of the induced Sm-*A* and *N* phases, bâtonnets of the former transform into edge-decorated disks above an applied electric field, and their characteristic features are similar to those described for the mixture in Ref. [5]. This shows that the edge decoration with a periodic pattern is a phenomenon that depends on the general properties of the smectic phase, and is not limited to any specific system. We develop here a simple theoretical model for its *threshold*, demonstrating that *saddle-splay elasticity* of the smectic can account for our observations, including the dependences of the number of undulations on the size of the disk and the applied field. The saddle-splay term [1,7] is essentially a surface term, playing an important role in director configurations in cylindrical and spherical geometries of nematics [8] and the stability of blue phases [9] of short pitched cholesteric LCs. In smectics, it describes the Gaussian curvature of the layers, and has been used to analyze focal conic structures [1]. The edge decoration of pristine Sm-*A* disks discussed in this paper is the most direct manifestation of saddle-splay elasticity in smectic LCs.

This paper is organized as follows. After describing the experimental set up in Sec. II, we present the results under Sec. III in two parts, of which, the first deals with the phase diagram of the system determined from optical and x-ray studies, and some unusual growth patterns of the N_{TB} nuclei; and the second, with the electric field effects on the induced Sm-*A* domains. Section IV is devoted to a theoretical analysis of the edge decoration of Sm-*A* disks. In Sec. V, we summarize the main results and their significance. The paper is supplemented by two videos and related notes; the latter also provide a description of several optical features of the observed phases not related to the saddle-splay instability; these are accessible in the Supplemental Material [10].

II. EXPERIMENTAL PROCEDURE

The dimer CB7CB used in this study was synthesized by two of the authors (M.B.K. and C.V.Y.). The phase sequence of CB7CB, from polarization microscopy, was: N_{TB} (103.3 °C) *N* (116.5 °C, T_{NI}) *I*; HOAB was a commercial sample having the phase sequence: Crystal, *Cr* (74 °C) Sm-*C* (94.8 °C) *N* (124.5 °C) *I*. Optical textures were obtained using a Carl-Zeiss Axio Imager.M1m polarizing microscope with an attached AxioCam MRc5 digital camera. The sample cells, procured from M/s AWAT, Poland, were sandwich type, constructed of ITO electrodes, coated with polyimide and buffed unidirectionally to ensure a uniform planar alignment of the nematic director **n;** the cell gap *L* was in the range 5–20 μm. Sample temperature *T*, accurate to ±0.1 °C, was maintained using an Instec HCS402 hot-stage coupled to a

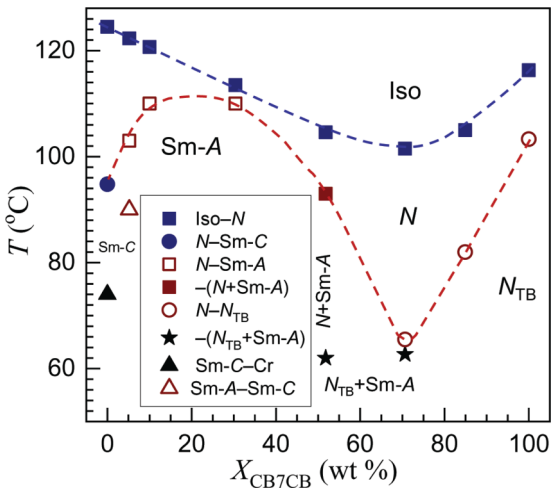

FIG. 1. Concentration *X* (wt. % of CB7CB) temperature phase diagram determined from x-ray diffraction and polarization microscopic studies. The *N* phase, common to all the studied mixtures, occurs over a temperature range that reaches a minimum for $X \approx 30$ and a maximum for $X \approx 70$. The Sm-*C* phase of pure HOAB is completely suppressed for $X > 5$; the Sm-*A* phase is induced in the concentration range 5–70; above $X \approx 70$, only the N_{TB} mesophase is observed below the nematic.

STC200 temperature controller. The driving voltage in electric field experiments was from a Stanford Research Systems function generator (DS345) coupled to a FLC Electronics voltage amplifier (model A800). A Keithley-2002 multimeter was used to measure the field frequency *f* and rms voltage *U*. x-ray measurements were performed using a PANalytical X'Pert PRO MP x-ray diffractometer comprising a focusing elliptical mirror and a fast high resolution detector (PIXCEL), the wavelength of the radiation being 0.15418 nm. The sample, contained in a glass capillary and kept in a Mettler hot-stage, was maintained at the desired temperature, accurate to ±0.1 °C. The diffraction data thus collected were analyzed using the Fityk profile fitting software [11]. For convenience, we use the following symbolic notations: the orthogonal reference axes *y* and *z* define the rubbing and observation/electric field directions, respectively; M_X denotes the binary mixture of CB7CB and HOAB with *X* wt. % of the former; $P(\alpha)$–$A(\beta)$ indicates the setting of the polarizer *P* and analyzer *A* with their axes at angles α and β (degrees) relative to *y*.

III. EXPERIMENTAL RESULTS

A. Phase diagram

Figure 1 shows the phase diagram for the CB7CB/HOAB system, arrived at from optical microscopic and x-ray studies. When the concentration *X* of CB7CB is high, as in M_{85} and M_{70}, expectedly, we observe the two nematic phases, *N* and N_{TB}, just as in pure CB7CB. The onset of the N_{TB} phase in both M_{85} and M_{70} is marked by the appearance of tactoidlike (in *plan view*) drops against a uniformly birefringent nematic background, as exemplified in Fig. 2(a). As the cooling progresses, the tactoidlike domains proliferate and grow, eventually to occupy the entire volume, giving a patchy colored texture. Thereafter, under decreasing fluidity,

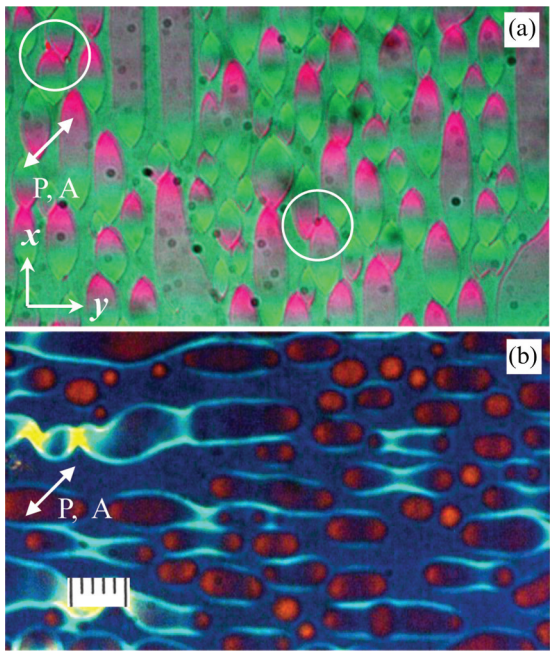

FIG. 2. (a) Tactoid-like N_{TB} drops nucleated at 64.8 °C within a nematic monodomain with the director **n** along y, in a 5-μm-thick sample of the mixture M_{70} ($X = 70.6$ wt. %). (b) The geometry of N_{TB} domains becomes circular in the Freedericksz reoriented state at 5 V, 1 kHz. Scale: 5 μm each subdivision.

the mixture passes into a characteristic defect state, previously described [12] as the *twin stripe* state from which the familiar arrays of parabolic focal conic domains (PFCDs) of the N_{TB} phase evolve. The sequence of textures leading to the PFCD state is shown in Fig. S1 of the Supplemental Material [10].

Some interesting optical features of N_{TB} drops [Fig. 2(a)] that relate to their director configuration may be noted. Clearly, from the extension of the drop orthogonal to the rubbing direction y, the anisotropy of interfacial tension $\Delta\gamma$ is negative and the optic axis at the N_{TB}-N interface lies along the surface normal. The drops are visible in ordinary light or linearly polarized light with the electric vector along y, but are almost extinct for the incident light vibrating along x. Thus, the optical axis in the N_{TB} domains lies predominantly in the yz plane. Interestingly, between diagonally crossed/parallel polarizers, the tactoidlike drops appear differently colored near their opposite vertices. Additionally, drops with the opposite color combination are also formed, as seen in the encircled regions of Fig. 2(a). These features are understandable from the shape of the N_{TB} drop taken to nucleate at one of the substrates (say, at the bottom one) and grow into the bulk. It will then be fully in contact at the bottom plate, while only its central part will be touching the top plate. A nonvanishing chirality in the drop generates different director profiles at the two tapering ends, leading to the optical dissimilarity. This aspect is elaborated in Fig. S5 and related discussion in the Supplemental Material [10].

In the biphasic N-N_{TB} region, which is limited to ~1 °C in M_{85} and ~2 °C in M_{70}, the two phases are readily distinguished by application of a suitable electric field $E = U/L$. At higher frequencies of E, at which the ionic effects become negligible, mixtures with positive $\Delta\varepsilon$—i.e., all the studied mixtures except M_5—show the Freedericksz transition at a threshold U_F, which is considerably lower for the N phase compared to the N_{TB} phase. For instance, in M_{70}, reorientation in the N region becomes discernible, through a change in interference color, at ~2 V. The N_{TB} drops, by comparison, show emphatic changes in color and geometry at ~$2U_F$; above this voltage, they tend to become circular with their optical axes along z, as in Fig. 2(b). At lower frequencies of the applied field, depending on the value of f, the nematic phase undergoes flexoelectric or electroconvective destabilization prior to the Freedericksz realignment (see Figs. S3 and S4, Supplemental Material [10], for details of different electrical effects).

While the mixture M_{85} crystallizes directly from the N_{TB} phase (at about 50 °C), M_{70} shows an additional mesophase before transforming to the crystal. At about 62 °C, within the PFCD state of M_{70}, elongated birefringent objects, identifiable as the well- known bâtonnets, begin to appear. The x-ray patterns recorded at various temperatures show the onset of a layered Sm-A phase at this temperature (Fig. 3, CB7CB 70%); the Sm-A, as usual, separates as bâtonnets, though in a multicomponent mixture of rod-like molecules with CB7CB, the bâtonnets have been attributed to the N_{TB} phase [12]. The Sm-A phase coexists with the N_{TB} phase over a wide range, extending till crystallization at about 49 °C. In the crystalline state, the two components of the mixture tend to separate (see Fig. S2, Supplemental Material, for related textures).

The Sm-A phase, not present in either of the components, is induced in all the mixtures with X_{CB7CB} in the range 5–70 wt. % (Fig. 3). As discussed in Sec. I, induction of the Sm-A phase in binary mixtures, with one component terminally strongly polar and the other relatively weakly polar or nonpolar, is known to be mainly due to the formation of charge transfer (CT) complexes [4,13]. CB7CB acts as an electron acceptor because of the CN groups that draw electrons from the aromatic core; HOAB, as the donor, interacts with CB7CB through CT complexing. Under a strong CT interaction, often, the induced smectic phase is found to be strongly stabilized, with the highest Sm-A–N transition temperature, for the molar mixing ratio 1:1. In the phase diagram for our system (Fig. 1), this maximum occurs for $X \approx 25$ wt. %, approximately corresponding to a CB7CB-HOAB molar ratio of 1:3. This may be attributed to the smectogenic nature of HOAB [4], and the *two* cyano groups in each CB7CB molecule.

In M_{50}, after the onset of the Sm-A phase in the form of usual bâtonnets (Fig. 4), the system remains biphasic even through crystallization. At lower temperatures, progressive decomposition takes place, with the CB7CB-rich N regions transitioning into the N_{TB} phase while the HOAB-rich bâtonnets remain in the Sm-A phase (Fig. S7, Supplemental Material). The mixtures M_{30} and M_{10} behave similarly in that the N_{TB} phase is completely eliminated in these, and the induced Sm-A follows the N (Fig. 1), with no other mesophase. The mixture M_5 differs from all the other mixtures in that it shows both Sm-A and Sm-C phases (Fig. 3).

B. Bâtonnets of the smectic-A phase in electric fields

When the N and Sm-A phases coexist, geometry of the Sm-A domains is influenced by the alignment of the nematic.

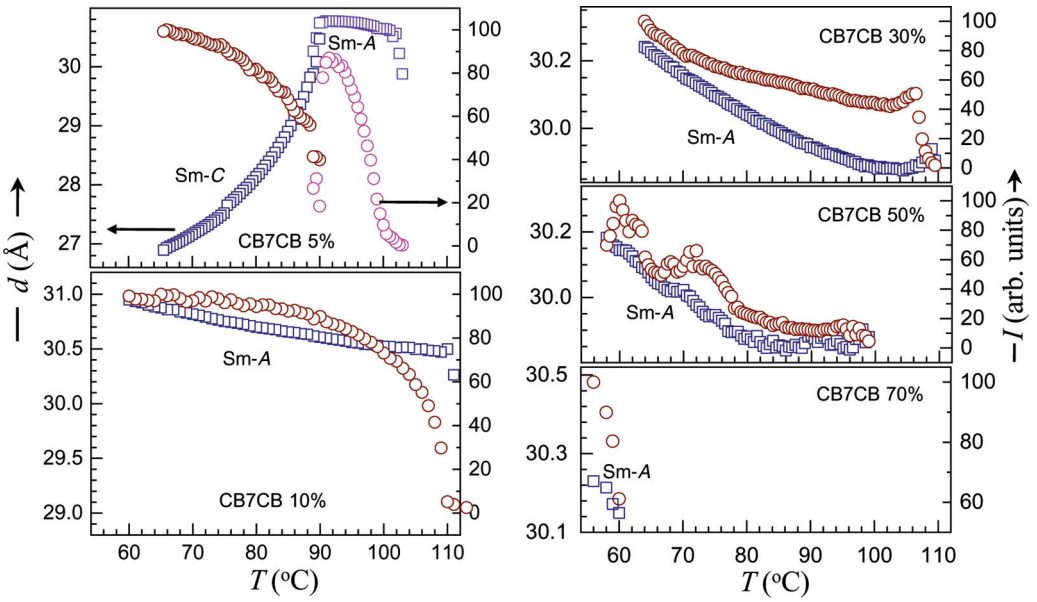

FIG. 3. x-ray measurements of the layer spacing d (left ordinate) and peak intensity I (right ordinate), for different compositions of the CB7CB/HOAB system in the temperature range 54−112 °C. No low angle scattering was observed for the mixture with 85% CB7CB. Squares and circles denote d and I, respectively. The marginal increase in Sm-A spacings with decreasing temperature is a result of chain stiffening.

In a (quasi)homeotropic nematic sample, smectic layers form parallel to the bounding surfaces and, because of the isotropic interfacial tension in the layer plane, their lateral boundary tends to be circular. This is readily verified in M_{50} or M_{30} by first applying a high frequency field with $U \gg U_F$ in the nematic phase, and then lowering the temperature into the N-Sm-A biphasic region. The unique feature of Sm-A disks thus formed is, as illustrated in Fig. 5, their undulatory boundary; the circular chain of bright spots of light seen in the peripheral region of the disks is due to the lens action arising from a periodic distortion of the director in this region. The focal planes of real and virtual images lying on either side of a Sm-A disk may be seen in the movie clip V1.avi available in the Supplemental Material [10].

When the electric field is applied after the onset of the Sm-A phase in a planar nematic, the bâtonnets of Sm-A, such as in Fig. 4, are affected only at higher voltages when the nematic is quasihomeotropic. In a 5-μm-thick layer of M_{52}, for example, the bâtonnets begin to undergo a major structural transformation only when U reaches around 16 V. The evolution of Sm-A disks (Fig. 5) from bâtonnets occurs in stages, as depicted in Fig. 6. The director reorientation in the N phase begins at ∼2.2 V; above 16 V, as in Fig. 6(c), bâtonnets transform into bands with circular terminations and corrugated long edges extending in the rubbing direction; the distortions in the interfacial region produce light focusing. The bands break up at higher voltages and the fragments assume the disk shape in time. Their wavy edge is well discerned by reducing the voltage slightly, as in Fig. 6(h) and 6(i). In M_{30}, the smectic disks form at focal conic defect sites (angular locations) of zigzag bâtonnets [Fig. 6(j)].

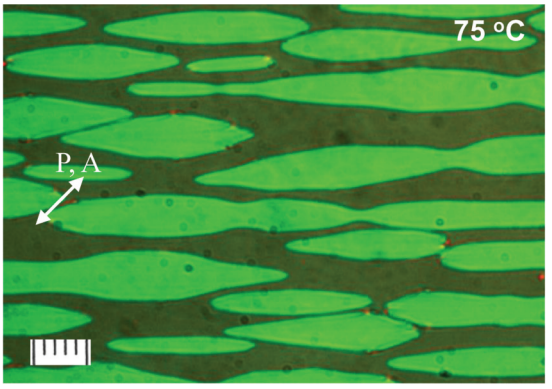

FIG. 4. Bâtonnets of the Sm-A phase coexisting with the N phase in a 5-μm-thick layer of M_{52}. Diagonally parallel polarizers. Scale: 5 μm each subdivision.

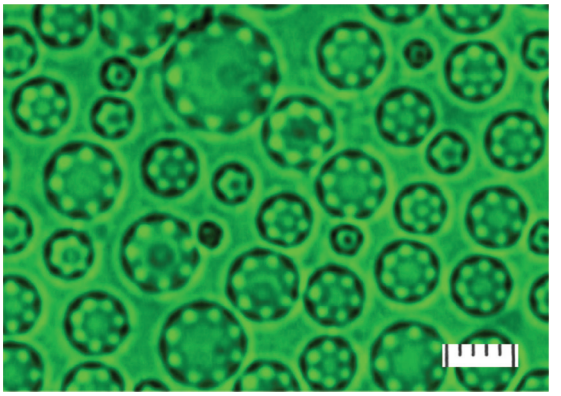

FIG. 5. Circular Sm-A domains formed deep in the Freedericksz state of a 20-μm thick, initially planar nematic sample of M_{50} at 85.5 °C, subjected to a field with $f = 10$ kHz and $U = 42$ V ($\approx 20\,U_F$) and observed using unpolarized mercury green light. Scale: 2 μm each subdivision.

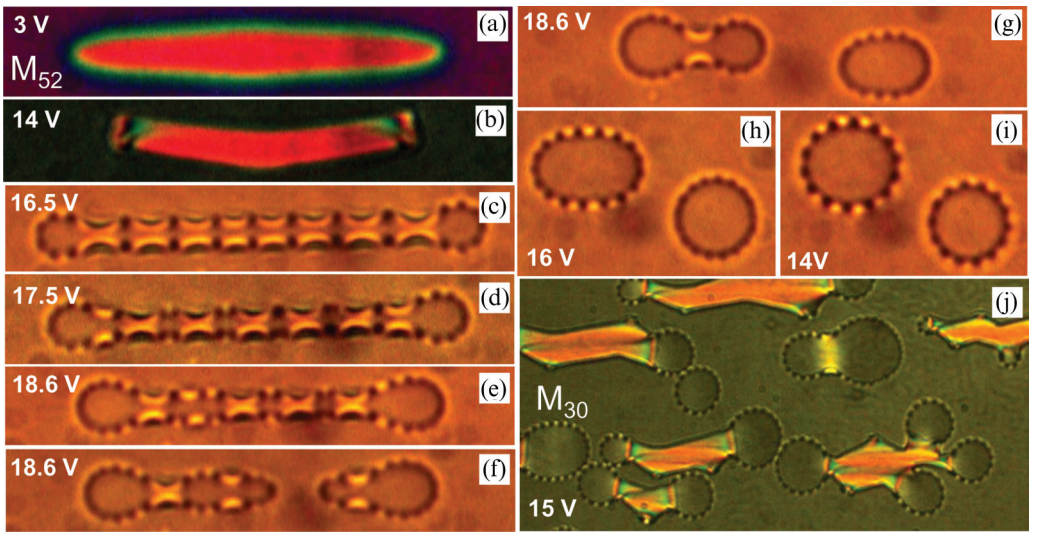

FIG. 6. (a)–(i) The course of transformation of Sm-*A* bâtonnets into homeotropic disks with corrugated boundaries under the influence of increasing electric field of frequency 1 kHz, in a 5-μm-thick layer of M_{52} at 86 °C. (j) Sm-*A* disks developing at angular locations of zigzag bâtonnets in M_{30} at 108 °C; 15 V, 1 kHz. $P(45)$–$A(135)$ in (a) and (b); $P(0)$ in (c)–(i); and $P(15)$–$A(135)$ in (j). $L = 5\,\mu$m.

The Sm-*A* disks change over to FCDs when the field strength falls below a critical value E_c. In a 5-μm thick-M_{52} layer at 85 °C, this happens for $U < 12$ V [(Fig. 7(e)]. As the voltage is reduced, the circular shape of the disks begins to appear more and more elliptical. The nucleation of FCDs begins, as a rule, at either or both of the two ends of the minor axis of the *apparent* ellipse, as in Figs. 7(f)–7(j) (see Supplemental Material [10] for a movie clip V2.avi that further illustrates this feature). By implication, the Sm-*A* disks are suspended in the nematic at higher fields; and, with reducing E, their normal, parallel to z at higher voltages, tends to tilt toward the rubbing axis y. This tilt

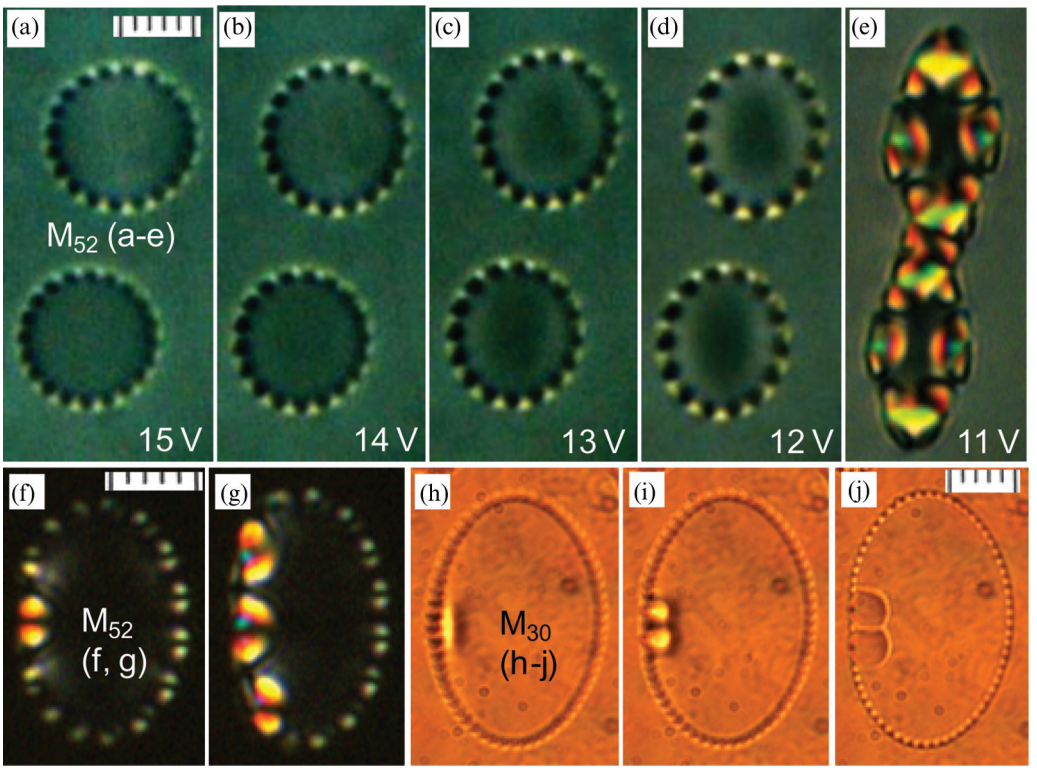

FIG. 7. Transformation of the near homeotropic state of Sm-*A* disks into focal conic defect state with reducing field of frequency 1 kHz. (a)–(e) Initially planar M_{52} layer; $L = 5\,\mu$m, $T = 85$ °C. Scale: 2 μm each subdivision. Progressive growth of FCDs from the left edge in contact with a substrate in (f), (g) $M52$ and (h)–(j) $M30$ (z-stacked images). Scale: (a)–(g) 2 μm each subdivision, (h)–(j) 5 μm each subdivision.

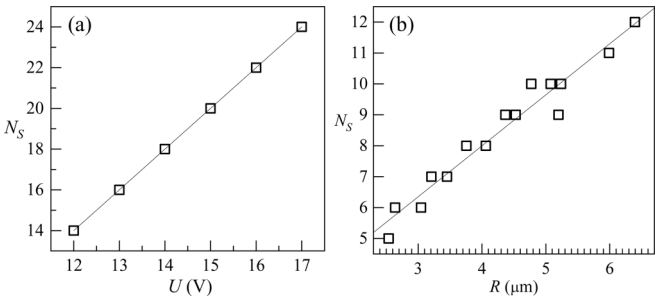

FIG. 8. Linear variation of the number of bright image spots N_S due to the undulatory edge of Sm-*A* disks as a function of (a) voltage of the sine wave field of frequency 1 kHz in a 5-μm-thick M_{52} sample at 85 °C and (b) radius of the disk in a 20-μm- thick M_{50} sample at 85.5 °C, subjected to a sine wave field with $U = 42$ V and $f = 10$ kHz.

would eventually bring a Sm-*A* disk into contact with either (or both) of the bounding surfaces, where the nucleation of FCDs is initiated and from where it spreads on either side.

The number of bright focal spots N_S at the boundary of a given homeotropic Sm-*A* disk varies with the field strength E. In the earlier study of similar smectic disks in Ref. [5], as already mentioned, $N_S(E)$ has been found to change slope at some field. We find it to be practically constant *close* to E_c and too small to be resolvable above some 4 V μm^{-1}. $N_S(E)$ is linear in the narrow voltage range between these limits [Fig. 8(a)]. At any given E, N_S also shows a linear dependence on the radius of the disk, as seen in Fig. 8(b).

IV. THEORETICAL ANALYSIS OF DECORATED SMECTIC *A* DISKS

The intensity variations at the edge of Sm-*A* disks imply that the layers are no longer flat there, but have a periodic distortion, which leads to light focusing effects. Any distortion costs elastic energy; and deviations of the director from the direction of the electric field cost dielectric energy as well. Indeed, one would normally expect that the disk, which is flat all the way up to the edge, would minimize the energy, and would be the equilibrium structure of the disk.

In order to develop a theoretical model for the decorated disk, it is useful first to consider a smectic sample of thickness $D = ml$, m being the number of layers, and l the layer thickness, with a *straight edge* (Fig. 9) lying in the yz plane. An electric field **E** acts along the layer normal, i.e., the z axis. Let there be a small uniform displacement u_o of the layers at the edge, tilting the director by an angle $\theta_o \approx n_x = -\partial u_o/\partial x$. As $\partial u_0/\partial z = 0$, we ignore the compression elastic constant in the present part of the analysis, and consider its influence later, when we discuss the structure of disks. The electric field tends to reduce $\theta(x)$ as we move away from the edge. If $\theta_o \ll 1$, the $\theta(x)$-dependent part of the free energy density is given by

$$F(x) = \frac{k_{11}}{2}\left(\frac{\partial\theta}{\partial x}\right)^2 + \left(\frac{\varepsilon_o \Delta\varepsilon E^2}{2}\right)\theta^2, \qquad (1)$$

where k_{11} is the splay elastic constant, ε_0 the vacuum dielectric constant, and $\Delta\varepsilon$ the (positive) dielectric anisotropy of

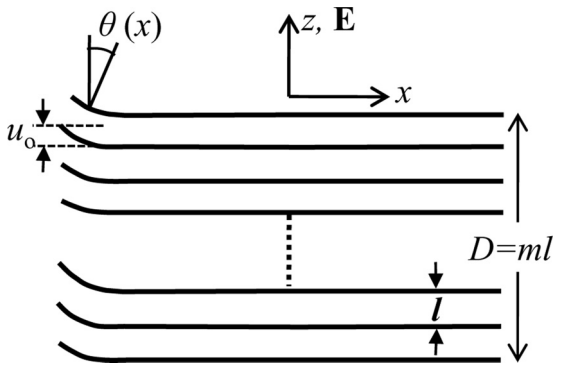

FIG. 9. Schematic of a Sm-*A* sample with thickness $D = ml$, where l is the layer spacing, and subjected to an electric field **E** acting along the layer-normal (z axis). A vertical displacement u_0 at the edge of the sample (lying in the yz plane) dies down along the x axis. $\theta(x)$ is the angle made by the layer-normal with the z axis.

the smectic sample. The Euler-Lagrange equation leads to the solution

$$\theta(x) = \theta_o e^{-x/\lambda}, \qquad (2)$$

where the length over which the deviation from the z axis of the layer normal (and hence the displacement u), decays due to the action of E is given by $\lambda = \sqrt{(k_{11}/\varepsilon_o\Delta\varepsilon)}/E$, being inversely proportional to E, as expected. Now let us assume that the edge displacement is sinusoidal along the y axis (Fig. 10), and given by $u(y) = u_o \sin(2\pi y/\lambda_y)$. The electric field tends to flatten the layers, and, in view of the result given by Eq. (2), we assume that a reasonable solution is given by

$$u(x, y) = u_o e^{-x/\lambda_x} \sin\left(\frac{2\pi y}{\lambda_y}\right). \qquad (3)$$

The x and y components of the director **n** are given by $n_x = -\partial u/\partial x$ and $n_y = -\partial u/\partial y$. To the leading order in u_o, the above solution is curl-free, as required in a smectic sample. Again ignoring the compression term, the displacement-dependent part of the free energy density reads as

$$F(x, y) = \frac{k_{11}}{2}\left(\frac{\partial n_x}{\partial x} + \frac{\partial n_y}{\partial y}\right)^2 + \left(\frac{\varepsilon_o \Delta\varepsilon\, E^2}{2}\right)\left(n_x^2 + n_y^2\right). \qquad (4)$$

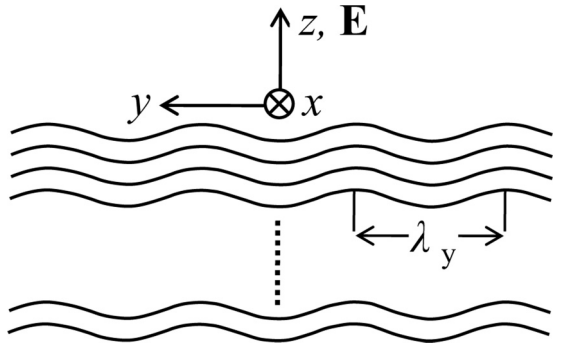

FIG. 10. Schematic diagram of a Sm-*A* sample with a sinusoidal undulation [given by Eq. (3)] imposed in the yz plane, lying in the plane of the page. An electric field E acts along the z axis.

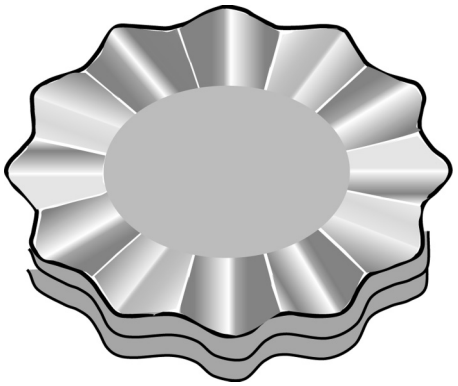

FIG. 11. Schematic diagram of a circular disk made of Sm-*A* layers, with a periodic undulation of the layers with an amplitude u_0 at the edge $r = R$. As discussed in the text, the amplitude dies down exponentially along the radial directions towards the center, and for clarity a slower decay is depicted in the figure. There is *no* periodicity of the radius R (though the perspective may seem to indicate such a structure).

Using the solution (3), we get

$$F(x,\ y) = u_o^2\, e^{-2x/\lambda_x}\left[\frac{k_{11}}{2}\sin^2\left(\frac{2\pi y}{\lambda_y}\right)\left(-\frac{1}{\lambda_x^2}+\frac{4\pi^2}{\lambda_y^2}\right)^2 + \frac{\varepsilon_o \Delta\varepsilon\, E^2}{2}\left(\frac{1}{\lambda_x^2}\sin^2\left(\frac{2\pi y}{\lambda_y}\right)+\frac{4\pi^2}{\lambda_y^2}\cos^2\left(\frac{2\pi y}{\lambda_y}\right)\right)\right]. \tag{5}$$

A remarkable feature of the above result is that, if the wavelength of the sinusoidal variation along the y axis satisfies $\lambda_y/2\pi = \lambda_x$, the net divergence itself amounts to 0, and there is no elastic energy cost associated with the distortion, and the dielectric energy density also becomes independent of the y coordinate. The splay cancellation due to opposite signs in different directions of the distortion has been noted earlier in some experiments on nematic LCs [14]. In the geometry considered above, the cancellation is total.

With this background, we can analyze the experimental results, which of course are on Sm-*A* *disks*, each with a well-defined radius and a finite volume. The Sm-*A* disk is suspended in the fluid nematic liquid crystal, and as in the previous example, we assume that the layer displacement u, and hence the director field has no z dependence in the disk. Using cylindrical polar coordinates (r, φ) appropriate for this geometry (Fig. 11), in analogy with Eq. (3), we assume

$$u(r,\varphi) = u_o e^{-(R-r)/\lambda_r}\sin\left(\frac{2\pi R\varphi}{\lambda_\varphi}\right), \tag{6}$$

where r is measured from the center of the disk with radius R, λ_r is the decay length of the edge distortion along $-r$, and λ_φ the wavelength of the sinusoidal edge distortion. We can also assume that there are an *integral* number of wavelengths around the periphery $\nu = 2\pi R/\lambda_\varphi$. If $\nu = 0$, $u(r,\varphi)$ is 0 everywhere, and the disk is perfectly flat. As such, $\nu \geqslant 1$ in the following. In the cylindrical coordinate system, the two independent components of the director $\mathbf{n}$ are

$$n_r = -\frac{\partial u}{\partial r} = -\frac{u_o}{\lambda_r}e^{-(R-r)/\lambda_r}\sin(\nu\ \varphi)$$

and

$$n_\varphi = -\frac{\partial u}{r\partial\varphi} = -\frac{u_o \nu}{r}e^{-(R-r)/\lambda_r}\cos(\nu\ \varphi). \tag{7}$$

The bulk free energy density, dependent on the distortions of n_r and n_φ can be written in analogy with Eq. (4). Again, to leading order in u_o, the distortion is *curl free*. In the cylindrical geometry,

$$\nabla\cdot\boldsymbol{n} = \frac{\partial n_r}{\partial r}+\frac{n_r}{r}+\frac{\partial n_\varphi}{r\partial\varphi} = u_o e^{-(R-r)/\lambda_r}\sin(\nu\ \varphi)\left[\left(-\frac{1}{\lambda_r^2}-\frac{1}{r\lambda_r}+\frac{\nu^2}{r^2}\right)\right]. \tag{8}$$

It is clear that unlike in the case of a sample with a straight edge, $\nabla\cdot\mathbf{n}$ cannot be 0 everywhere in a disk. Further, as the disk has a lateral *free* surface, we have to take into account the effect of another term involving $\nabla\cdot\mathbf{n}$, viz., the saddle-splay elasticity. In Sm-*A* LCs, it also describes the elasticity associated with the Gaussian curvature of the layers [1], while the k_{11} term describes that related to their mean curvature. Our analysis will be restricted to terms only upto $u_o{}^2$ in the free energy, i.e., to the *threshold* of the instability. As $\nabla\times\mathbf{n} = 0$ to leading order in u_o, the energy density due to saddle-splay reduces to $k\nabla\cdot(\mathbf{n}\nabla\cdot\mathbf{n})$. (Some authors adopt the opposite sign convention [7].) Further, by the Gauss theorem, the contribution to the total free energy due to this term can be written as the following surface contribution:

$$G_\kappa = D\kappa\int_0^{2\pi} R\, n_r \nabla\cdot\boldsymbol{n}\, d\varphi = \pi\ \kappa D\, u_o^2\frac{R}{\lambda_r}\left(\frac{1}{\lambda_r^2}+\frac{1}{R\lambda_r}-\frac{\nu^2}{R^2}\right), \tag{9}$$

which is calculated at the surface of the edge at $r = R$. We may note that a negative saddle-splay coefficient k forces the terms in brackets of Eq. (9) to add up to a large positive value for $\nu = 0$, i.e., it does not lead to undulations. The positive sign of κ, which favors a negative Gaussian curvature, is consistent with the occurrence of the FCDs of type I mentioned earlier [1,5].

Before we proceed further, we recall that an undulation structure which is geometrically similar to the one studied in this paper was found in a very different physical system [15]. Polystyrene spherical beads, each with a diameter of 2.8 μm, deposited on free standing Sm-*A* films were found to generate a corona region (of width $\sim$4−5 μm) around the bead, with an azimuthally periodic undulation. The origin of the structure was found to involve (i) wetting of the bead with a relatively large surface tension by the Sm-*A* LC, which resulted in (ii) a meniscus region forming the corona, with a thickness decreasing away from the bead, and (iii) the curvature of the meniscus generating a tensile stress and the periodic undulation instability seen in the experiment. Analogous undulating structures have been directly visualized in the meniscus regions formed close to the solid walls around circular holes across which the free standing films of other types of smectic LCs have been studied [16,17]. In most parts

of the undulating structure in the meniscus $\partial u/\partial z$ is nonzero, and the theoretical analysis necessarily takes into account the compression elasticity (B) of the smectic. In the cylindrically symmetric system, the relevant contribution to the free energy density is given by

$$F_B(r,\varphi) = \frac{B}{2}\left(\frac{\partial u}{\partial z} - \frac{1}{2}\left(\left(\frac{\partial u}{\partial r}\right)^2 + \frac{1}{r^2}\left(\frac{\partial u}{\partial \varphi}\right)^2\right)\right)^2, \quad (10)$$

in which the higher order term arises from the tilting of the layers.

It is immediately clear that the Sm-A disks studied by us are rather different, each with a *constant* number of layers with a fixed volume, *without* any connected reservoir, meniscus with variable thickness or tensile stress. The disks are perhaps the simplest stand-alone Sm-A structures studied. $\partial u/\partial z = 0$ for the layer displacement field $u(r,\varphi)$ given by Eq. (6) and the compression term given by Eq. (10) contribute to the energetics only through the fourth order term $\propto {u_0}^4$, arising from the tilt of the layer, and hence does not figure in the calculation of the threshold. We will later make some remarks about the effect of the B term above the threshold.

The Sm-A disk has two types of interface with the surrounding medium. We will assume at first that the Sm-A disk is surrounded by the isotropic phase, and consider the more complicated case of the nematic LC later. At the edge, at R, the liquid layer of Sm-A is in contact with the isotropic medium, and the corresponding interfacial tension $\gamma_\perp$ is smaller than $\gamma_\parallel$ for the top and bottom interfaces of the disk. An area element at the *edge* is

$$dA_E = RD\sqrt{1+\left(\frac{\partial u}{R\partial\varphi}\right)^2}\, d\varphi. \quad (11)$$

As $u_o \ll R$, the total area of the undulating edge is

$$A_E = 2\pi RD\left(1+\frac{u_o^2\nu^2}{4R^2}\right). \quad (12)$$

An area element at the *top surface* of the disk is

$$dA_T = \sqrt{1+\left(\frac{\partial u}{\partial r}\right)^2+\left(\frac{\partial u}{r\partial\varphi}\right)^2}\, r dr\, d\varphi. \quad (13)$$

The total area of the top surface is

$$A_T = \pi R^2\left(1+\frac{u_o^2}{2R^2}\int_0^R e^{-2(R-r)/\lambda_r}\left(\frac{\nu^2}{r}+\frac{r}{\lambda_r^2}\right)dr\right). \quad (14)$$

Our aim is to compare the free energies of Sm-A disks with and without any undulations of equal volume. As the number of layers and hence the thickness D is unaltered, the top surface area A_T should be equal in the two cases, i.e., $A_T = \pi {R_F}^2$, where R_F is the radius of the undulation-free flat disk. The extra interfacial area of the undulated disk is $\Delta A_E = A_E - 2\pi R_F D$, the latter being the edge area of the flat disk:

$$\Delta A_E = \frac{\pi D u_o^2}{2R}\left(\nu^2 - \int_0^R e^{-2(R-r)/\lambda_r}\left(\frac{\nu^2}{r}+\frac{r}{\lambda_r^2}\right)dr\right). \quad (15)$$

Keeping terms only up to ${u_o}^2$, we can now write the excess free energy of an undulated disk compared to that of a flat one with an equal volume as

$$\Delta F_{\rm sm} = \left[D\left\{\int_0^R\int_0^{2\pi}\left(\frac{k_{11}}{2}(\nabla\cdot\mathbf{n})^2 + \frac{\varepsilon_o\Delta\varepsilon E^2}{2}\left(n_r^2+n_\varphi^2\right)\right) r\, dr\, d\varphi\right\} + G_\kappa + \gamma_\perp\Delta A_E\right], \quad (16)$$

where n_r and n_φ, $\nabla\cdot\boldsymbol{n}$, G_k, and $\Delta A_{\rm E}$ are given by Eqs. (7)–(9), and (15), respectively. If $\Delta F_{\rm sm}$ is negative, the undulated structure is favored.

To a good approximation, λ_r may be expected to be given by the expression for λ shown after Eq. (2). The only negative contribution to $\Delta F_{\rm sm}$ arises from saddle-splay elasticity, which drives the undulation instability at the edge of the disk. It is usually stated that for the layers themselves to be flat, or the nematic director $\mathbf{n}$ to be undistorted in the ground state, the magnitude of κ should not be larger than that of k_{11} (The Ericksen inequality [1]). There are only a few measurements of κ in the nematic LC, but the uncertainties in the earlier measurements [8] are too large to confirm this result. A recent measurement on cylindrical samples of a chromonic nematic LC [18] yields $\kappa \approx 55k_{22}$ (the twist elastic constant) and $\kappa \approx 5k_{33}$ (the bend elastic constant), both of which violate strongly the Ericksen inequality. The authors have argued that the large value of κ does not violate the thermodynamic equilibrium of the structure. We may also note that the Ericksen inequality is based on assuming a *uniform* distortion of the sample, while practically in all experimental systems including ours, the distortion is distinctly nonuniform. We have made calculations using the following parameters: $\Delta\varepsilon = 1$, $k_{11} = 40\,$pN, $\kappa = 200\,$pN and $\gamma_\perp = 10\,\mu$J/m^2. The integrands $\propto r^{-2}$ and r^{-3} in the k_{11} part tend to diverge at $r = 0$, and we use the lower limit of all integrals to be $0.01R$, and as $\lambda_r \ll R$, the integral values are insensitive to the actual (small) value of the chosen lower limit.

We show in Fig. 12 all the four contributions as well as the total $\Delta F_{\rm sm}$ of Eq. (16) as functions of ν, the number of undulations around the periphery for a disk with $R = 5\,\mu$m subjected to an electric field $E = 4.76\,$V/μm. As the different contributions to $\Delta F_{\rm sm}$ depend linearly on D, the thickness of the disk, the free energy itself simply scales linearly with D which is chosen to be 2 μm in the calculations. The free energy near the threshold scales as ${u_o}^2$ and the amplitude u_o of the distortion is assumed to be 5 nm for the illustrative calculations.

The decay length λ_r ($= 0.447\,\mu$m) is fixed by the field E. The saddle-splay energy G_κ given by Eq. (9) is also positive

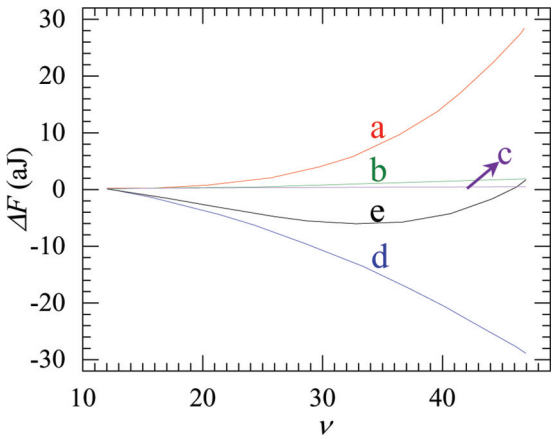

FIG. 12. Different contributions to the free energy (in atto J) of a Sm-A disk, with a radius of 5 μm surrounded by isotropic phase, and under the action of an electric field $E = 4.76\,\mathrm{V}/\mu\mathrm{m}$, as functions of ν, the number of undulations at the edge. The positive splay elastic energy [curve (a) at $\nu = 45$] rapidly increases for $\nu > 20$, and the dielectric energy [curve (b)] shows a small increase with ν. The interfacial energy [curve (c)] is very small, and stays close to 0 compared to the other contributions. The saddle-splay contribution [curve (d)], which is negative, sharply increases in magnitude with ν. The total free energy [curve (e)] has a minimum at $\nu = 34$.

up to $\nu = 11$. The splay elastic term, the dielectric and the excess edge energy contributions increase with ν, though the interfacial energy is rather small compared to the other contributions and just hovers above 0 in the vertical scale used in Fig. 12. The negative energy due to saddle splay increases in magnitude with ν if it is $\geqslant 12$, reflecting that of the net negative Gaussian curvature of the layers. The total free energy ΔF_{sm} itself becomes negative for $\nu = 13$, exhibits a *minimum* at $\nu = 34$, and becomes positive again for $\nu \geqslant 46$. The main competition is between the positive splay and negative saddle-splay terms. At intermediate values of ν, a partial splay compensation discussed earlier ensures that the relevant energy is quite low (Fig. 12), and the negative saddle-splay term dominates. At higher values of ν (above about 20), after moving away from the splay compensation regime, the splay term that depends on ν^4 increases faster than the saddle-splay term $\propto \nu^2$, resulting in the minimum in total energy. Thus the model predicts that the equilibrium structure of the disk has 34 edge undulations. The corresponding $\lambda_\varphi = 2\pi R/\nu = 0.924\,\mu$m is more than twice $\lambda_r = 0.447\,\mu$m.

In the experiments, the Sm-A drop is surrounded by nematic liquid crystal, and the electric field above which the disks form (applied RMS voltage $\sim$20 V, the sample thickness being 5 μm) is well above that corresponding to the Freedericksz (voltage) threshold of the nematic ($\sim$2 V). An interesting experimental observation is that when E is reduced from a higher value, apart from a reduction in the number of bright spots, the disk takes an elliptic shape at some E, and the aspect ratio of the ellipse increases as the field is decreased (Fig. 7). This can be understood as a *tilting* of the disk, when the nematic director around the disk itself tilts in the central part of the cell, generating a torque on the disk (Fig. 13). Indeed between crossed polarizers set at 45° to the rubbing direction, the elliptic drop brightens as the principal axes of the refractive index ellipsoid of the disk also tilt. Below some lower value of E, the disk touches the glass plates of the cell, and the director reorientation along the rubbing direction of the walls gives rise to focal conic textures (Fig. 7). This observation also implies that the nematic director is *strongly anchored at the interface*, and can be assumed to have the same orientation as that of the smectic, with a maximum deviation from the z axis at the lateral interface. As in the smectic drop, moving away from the interface, the electric field reorients the nematic director along **E**. The elastic deformation and the deviation of **n** from **E** in the surrounding nematic, which also cost energy, have to be taken into account. As can be visualized from Fig. 11, there are three *different* types of director distortion in the nematic, depending on its location in the vicinity of the Sm-A disk. The free energy *density* of the nematic of a given type i arising from elastic and dielectric contributions can be written, in general, as

$$F_n(i) = \frac{k_n}{2}[(\nabla\cdot\mathbf{n})^2 + (\mathbf{n}\cdot\nabla\times\mathbf{n})^2 + (\mathbf{n}\times\nabla\times\boldsymbol{n})^2] + \frac{\varepsilon_o\Delta\varepsilon_n E^2}{2}\left(n_r^2 + n_\varphi^2\right), \tag{17}$$

where for simplicity we have assumed the one elastic constant approximation with $k_n = k_{11} = k_{22} = k_{33}$, and $\Delta\varepsilon_n$ is the dielectric anisotropy of the nematic LC. We can now calculate the contributions from the three regions of the nematic.

Region a: This is the nematic radially extending from the edge of the disk, with $r > R$ and its thickness D being the same as that of the disk. The director deformation from the lateral edge of the disk dies down exponentially as the radius increases in the nematic, and as in the case of Sm-A at $r < R$, we can assume that the distortion has no z dependence. The radial and azimuthal components of the director are then given

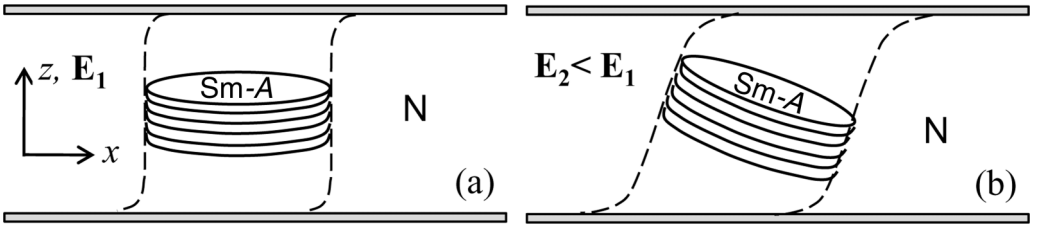

FIG. 13. Schematic of a Sm-A disk (a) at higher voltages [as in Fig. 7(a), for $E = 3\,\mathrm{V}/\mu\mathrm{m}$], with its normal along E; and (b) at lower voltages [as in Fig. 7(d), for $E = 2.4\,\mathrm{V}/\mu\mathrm{m}$], with its normal tilted relative to E. The N director remains strongly anchored to the Sm-A director at the interface.

by

$$n_r(r,\varphi) = -\frac{u_o}{\lambda_r} e^{(R-r)/\lambda_{\rm rn}} \sin\ (\nu\varphi)$$

and

$$n_\varphi(r,\varphi) = -\frac{u_o \nu}{R} e^{(R-r)/\lambda_{\rm rn}} \cos\ (\nu\varphi), \tag{18}$$

in which the director orientation agrees with that of the smectic disk at the interface when $r = R$, and the decay length in the nematic is given by

$$\lambda_{\rm rn} = \sqrt{k_n/\varepsilon_o \Delta\varepsilon_n}/\ E. \tag{19}$$

Unlike in the Sm-*A* disk, $\nabla \times \mathbf{n}$ is no longer 0 in the nematic and the contribution to the total free energy of the region *a* of the nematic is given by

$$\Delta F_n(a) = D \int_0^{2\pi} d\varphi \int_R^{R+m\lambda_{\rm rn}} r dr F_n(a), \tag{20}$$

where $m \sim 5$ ensures that the director deviation from the z-axis would be negligible for larger values of r.

Region *b*: This is the region of nematic lying above and below the Sm-*A* disk from $r = 0$ to $r = R$. The director components can be written as

$$n_r(r,\varphi,z) = -\frac{u_o}{\lambda_r} e^{-(R-r)/\lambda_r} \sin\ (\nu\varphi) e^{-z/\lambda_z}$$

and

$$n_\varphi(r,\varphi,z) = -\frac{u_o \nu}{r} e^{-(R-r)/\lambda_r} \cos\ (\nu\varphi) e^{-\frac{z}{\lambda_z}}, \tag{21}$$

where z is measured from the top surface of the disk along the positive z axis, and the above director field agrees with the one in the Sm-*A* disk when $z = 0$. In the one constant approximation used, $\lambda_z = \lambda_{\rm rn}$. The energy due to the part *b* of the nematic is given by

$$\Delta F_n(b) = 2 \int_0^{2\pi} d\varphi \int_0^{R} r dr \int_0^{m\lambda_z} dz F_n(b). \tag{22}$$

The factor 2 takes care of both the nematic regions above and below the disk.

Region *c*: This is the nematic lying above and below the nematic region (*a*). The components of the director are

$$n_r(r,\varphi,z) = -\frac{u_o}{\lambda_r} e^{(R-r)/\lambda_{\rm rn}} \sin\ (\nu\varphi) e^{-z/\lambda_z},$$

and

$$n_\varphi(r,\varphi,z) = -\frac{u_o \nu}{R} e^{(R-r)/\lambda_{\rm rn}} \cos\ (\nu\varphi)\ e^{-\frac{z}{\lambda_z}}, \tag{23}$$

which reduce to those in the region *a* when $z = 0$. The contribution from this region to the free energy of the medium is given by

$$\Delta F_n(c) = 2 \int_0^{2\pi} d\varphi \int_R^{R+m\lambda_{\rm rn}} r dr \int_0^{m\lambda_z} dz F_n(c). \tag{24}$$

The factor 2 takes care of both the top and bottom parts of this nematic region.

The total free energy of the smectic and nematic regions in relation to that of the undistorted flat disk is given by

$$\Delta F_{\rm tot} = \Delta F_{\rm sm} + \Delta F_n(a) + \Delta {\rm F}_n(b) + \Delta F_n(c). \tag{25}$$

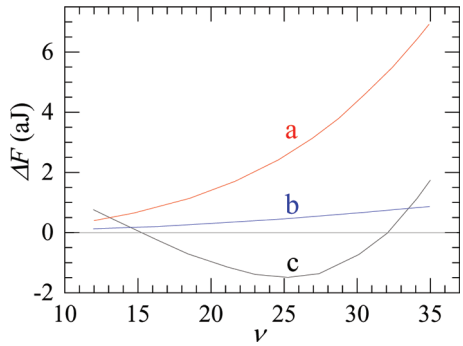

FIG. 14. The total contributions from all the three regions of the nematic LC as described in the text to the elastic energy [curve (a) at $\nu = 20$], and the dielectric energy [curve (b)] added to $\Delta F_{\rm sm}$ give rise to a minimum at $\nu = 25$ [curve (c)].

We have assumed $k_n = 20$ pN, and $\Delta\varepsilon_n = 1$, the latter being the same as for the Sm-*A* LC. The *sums* of the contributions from all the three nematic regions to both the elastic and dielectric energies increase with ν, as shown in Fig 14. The total free energy $\Delta F_{\rm tot}$ exhibits a shallower minimum compared to that of $\Delta F_{\rm sm}$, and at a *lower* ν, which is reduced to 25 (Fig. 14), corresponding to $\lambda_\varphi = 1.26\,\mu$m.

As the contributions from the regions *b and c* of the surrounding nematic are independent of thickness D, the total free energy depends on D unlike for a Sm-*A* disk surrounded by the isotropic phase. The dependence is, however, weak. For $R = 5\,\mu$m and $E = 4.756\,{\rm V}/\mu$m, $\nu = 25$ when $D = 2\,\mu$m, and $\nu = 24$ when $D = 1\,\mu$m. Reducing the saddle-splay elastic constant κ to 150 pN from 200 pN lowers the equilibrium value of ν to 21, for $D = 2\,\mu$m. Reducing κ to 100 pN, the free energy minimum is positive even for $E = 6.726\,{\rm V}/\mu$m. Thus, as in the case of chromonic nematics, the saddle-splay constant of the induced Sm-*A* LCs is $\gtrsim$4 times k_{11}.

The experimentally observed bright spots around the periphery of the disks arise from focusing effects. In the uniaxial Sm-*A* and *N* LCs, the refractive index μ_e for a light beam polarized along the director is larger than μ_o for the orthogonal polarization. At any given position (r, φ) the beam splits into the two polarized components, with the effective extraordinary index $\mu_{\rm eff} \approx \mu_o[1 + 0.5\theta^2(\mu_e{}^2 - \mu_o{}^2)/\mu_e{}^2]$ slightly larger than μ_o, θ being the angle made by the director with the z axis. From Eq. (7), the projected director $n_\perp = \sqrt{(n_r^2 + n_\varphi^2)} \approx \theta$ has a nonzero value at all azimuthal orientations φ at any given r, but the exponential decays of θ along the radial direction on both sides of the edge focus the light towards the periphery. The edge undulations of the experimentally studied disks are well developed, i.e., u_0 is not negligible unlike in the theoretical analysis. The orientational order and hence μ_e of Sm-*A* can be assumed to be larger than that of the surrounding NLC. Including those in the nearby NLC, the proposed deformations of the director field are three-dimensional, but it is clear that, near the edge, the Sm-*A*–*N* interface is *tilted*; and when a light beam enters the Sm-*A* drop, in general, it is refracted at the interface. The beam entering *around the trough* of the undulation is refracted *towards* the central beam from all the three Sm-*A*

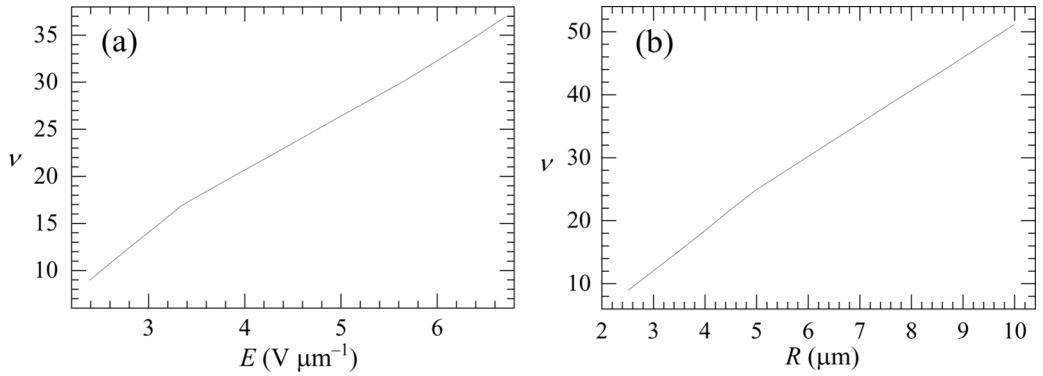

FIG. 15. (a) Theoretical variation of ν with E in a Sm-A disk with $R = 5\,\mu$m as described in the text. The essentially linear dependence reflects that seen in experiments (see Fig. 8(a) above and Fig. 8 in Ref. [5]). (b) The dependence of ν on the radius of the disk R, fixing $D = 2\,\mu$m, $E = 4.756\,\mathrm{V}/\mu$m and $\kappa = 200$ pN. The dependence is linear, as seen experimentally in both the experimental systems (see Fig. 8(b) above and Ref. [5]). This simply implies that λ_φ is determined mainly by the decay lengths as long as the radius R of the disk is considerably larger than those lengths.

regions (with $r < R$ and φ larger and smaller than that at the trough). The deviations get *enhanced* in the Sm-A due to the gradient in μ_{eff}. On the other hand, near the *crests* of the undulation, the refraction at the interfaces tilts the beams *away* from the central beam, though the gradients in μ_{eff} push them back towards the central beam. Thus the final focusing effect depends on the relative magnitudes of the two effects. If u_0 is large enough, the large interfacial refraction focuses the light beams strongly above the troughs and the number of bright spots $N_S = \nu$, the number of undulations. This seems to be the case in the system studied in this paper, and we can also see odd number of bright spots, depending on E and R (Figs. 5 and 8). If u_0 is relatively small, the interfacial refraction cannot be large, and the light beams near *both* troughs and crests of the undulation get focused because of the gradients in μ_{eff}, and $N_S = 2\nu$. This appears to be the case in the system studied in Ref. [5], where only even values of N_S were recorded in well-developed disks.

The dependence of the equilibrium value of ν as a function of the applied electric field E is shown in Fig. 15(a) for $\kappa = 200$ pN, $D = 2\,\mu$m, and $R = 5\,\mu$m**.** It is essentially linear (apart from a slightly sharper variation at low values of E), as seen in experiments. In the system studied in Ref. [5], the slope of the variation increases beyond $E \approx 6\,\mathrm{V}/\mu$m, which is not seen in our calculations, which are only valid close to the threshold of the instability. Nevertheless, the slope of the curve is similar to those in the two experimental systems within a factor of about 2. The decay lengths (λ) are $\propto 1/E$, and the total ν-dependent elastic energies can overtake the variation in the magnitude of the saddle-splay energy at a lower value of ν or a higher λ_φ as E is reduced, corresponding to an optimum net Gaussian curvature. The minimum free energy has a *positive* sign when E is lowered to $2.38\mathrm{V}/\mu$m, and the undulation structure is *metastable*. The decay length λ_{r} corresponding to $E = 2.38\,\mathrm{V}/\mu$m is 1.26 μm, and as the distortion covers a relatively large fraction of the area of the disk, the unfavorable dielectric and splay elastic energies prevail for all values of ν. However, to reach the stable uniformly oriented disk, ν has to decrease, which increases the energy, and the potential barrier can ensure that the structure is stuck in the deformed state.

The dependence of ν on the radius of the disk R, for $D = 2\,\mu$m, $E = 4.756\,\mathrm{V}/\mu$m, and $\kappa = 200$ pN, is shown in Fig. 15(b). The dependence is essentially linear, as seen in both the experimental systems. This simply implies that λ_φ is determined mainly by the decay lengths as long as the radius R of the disk is considerably larger than those lengths.

Above the threshold, as u_0 increases, the fourth order term of Eq. (10) has to be included in Eq. (16) and Eq. (24). In addition, the following destabilizing dielectric term contributes at this order: $-\varepsilon_0\Delta\varepsilon E^2\{(\partial u/\partial r)^4 + (\partial u/\partial\varphi)^4/r^4\}/6$. Very roughly this contribution renormalizes the B coefficient of Eq. (10) at the fourth order as $(B - \varepsilon_0\Delta\varepsilon E^2)$. As the maximum electric field applied is below $\sim 10\,\mathrm{V}/\mu$m, the effective value of B can be treated as a constant.

A very rough estimate shows that the compression elastic energy density becomes comparable to the splay contribution when $Bu_0^2 \geqslant 10k_{11}$. As the disks are formed in the two phase coexistence range, B can be expected to be relatively small, $\leqslant 10^6\,\mathrm{J/m^3}$. The two energies become comparable for $u_0 \sim 10$ times the layer spacing. It is clear that the contribution from B shifts the equilibrium value of ν to a lower value. A higher value of the electric field increases ν [Fig. 15(a)]. Further, the stronger dielectric torque [see Eq. (16)] can be expected to reduce the value of u_0, i.e., push the structure towards the threshold, reducing the effect of the B coefficient. This may account for the enhancement of the slope of the $\nu(E)$ curve at higher values of E in Ref. [5].

V. CONCLUSIONS

The experimental observation of a pristine Sm-A disk which is immersed in a nematic medium and mainly stabilized by the action of a large enough electric field on the positive dielectric anisotropy of the medium is by itself interesting. The development of the undulation instability near the edge of such a disk, which is visible in an optical microscope is a novel effect caused by the saddle-splay elasticity of the Sm-A LC. From the earlier discussion, it would be interesting to look for this effect in other geometries.

When a sample is taken in a cell whose walls are treated for homeotropic anchoring and cooled to the coexistence range,

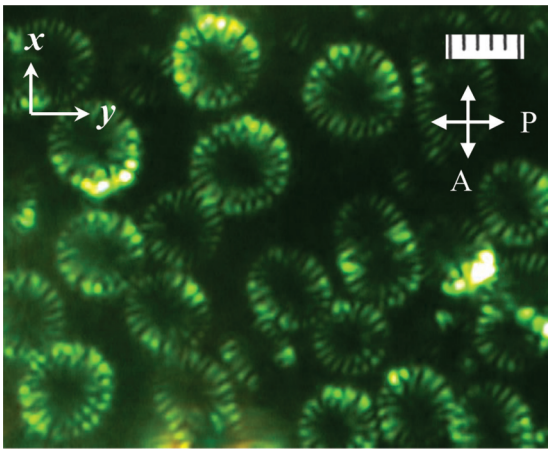

FIG. 16. Sm-*A* domains formed in the homeotropic nematic phase in a 9-μm-thick layer of M_{50} at 84 °C. Scale: 2 μm each subdivision.

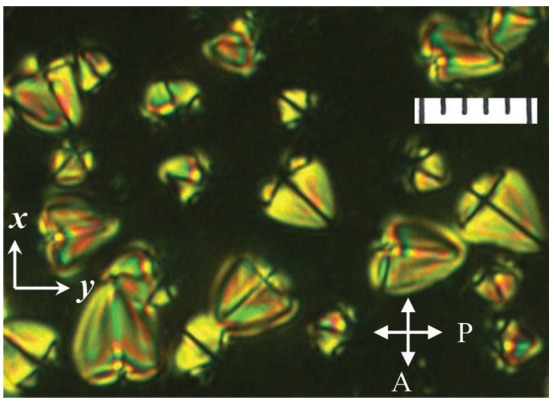

FIG. 17. Focal conic domains of the Sm-*A* phase formed in the homeotropic nematic phase in a 9-μm-thick layer of M_{50}. Scale: 5 μm each subdivision.

nearly circular Sm-*A* disks nucleate on the (lower) treated surface (Fig. 16). These disks present slightly elongated bright bands oriented towards their centers, reminiscent of the spots exhibited by disks formed under a strong electric field in cells treated for planar alignment. In several of them, there appears to be an inner ring of bright spots, separated from the outer one by a small gap. This probably indicates that a second smaller disk has grown on the on top of the disk resting on the plate. As the temperature is lowered further, Sm-*A* nuclei form in the center of the cell as well, which avoid the higher interfacial energy across the layer normal-nematic interface by bending of layers to form focal conic domains (Fig. 17).

As in the case of the disks formed by the action of electric field, the saddle-splay elasticity generates periodic undulations at the edge of the disk. This results in angular deviations ($\ll 1$ rad) of the director from the easy axis along z on the surface treated for homeotropic anchoring, and costs an anchoring energy per unit area given by $w \sin^2\theta/2$. As the top surface of the Sm-*A* disk has no restraints, all the layers in the disk undulate in unison, i.e., $\partial u/\partial z = 0$, as before. The undulation amplitude decays towards the center of the disk, the decay length now given by $\lambda_w = k_{11}/w$. With a typical anchoring strength $w \sim 10^{-4}$ J/m^2 and $k_{11} = 40$ pN as before, the decay length λ_w is 0.4 μm, similar in magnitude to the decay lengths dictated by the dielectric interaction with E. Consequently, as in the earlier case, the edge decorated disks are stabilized by the saddle-splay elasticity of Sm-*A* LC (In the system studied in Ref. [5], due to the chemical nature of the components, Sm-*A* did not nucleate on the surface treated for homeotropic anchoring, and only formed focal conic domains in the center of the cell).

There is a report of a disk shaped monolayer of *chiral* fd virus particles floating on water exhibiting periodic distortions that grow in the form of twisted ribbons, if the edge interfacial energy is reduced by polymeric depletants [19]. The saddle-splay term has been invoked to understand the structure. The cubic bicontinuous phase in lyotropic liquid crystals in the dilute regime is again a consequence of the negative Gaussian curvature of the layers [20]. Other structures have been proposed theoretically, which are stabilized by interfaces [21]. The system discussed in the present paper is an unusual example of the influence of saddle-splay elasticity, which is manifest because of (i) a relatively low value of the splay elastic energy due to partial splay cancellation at large values of the azimuthal wavelength λ_φ (or low values of ν), and (ii) a very small value of the interfacial tension that cannot suppress the edge distortion. Though circularly shaped *islands* have been found on free standing films of Sm-*A* LC, they do not exhibit the undulation instability, as it is suppressed by the large surface tension of about 20 mN/m [22], which is three orders of magnitude higher than in the systems discussed in this paper.

ACKNOWLEDGMENTS

The authors are grateful to Prof. G. U. Kulkarni for the experimental facilities; C.V.Y. acknowledges the financial support from Science and Engineering Research Board (SERB), Department of Science and Technology (DST), Government of India, under Project No. EMR/2017/000153.

[1] M. Kleman and O. D. Lavrentovich, *Soft Matter Physics: An Introduction* (Springer, New York, 2003).
[2] J. B. Fournier and G. Durand, J. Phys. II France **1**, 845 (1991).
[3] P. Oswald and P. Pieranski, *Smectic and Columnar Liquid Crystals* (Taylor and Francis, London, 2006).
[4] W. H. de Jeu, L. Longa, and D. Demus, J. Chem. Phys. **84**, 6410 (1986).
[5] R. Pratibha and N. V. Madhusudana, Physica A **224**, 9 (1996).
[6] M. Cestari, S. Diez-Berart, D. A. Dunmur, A. Ferrarini, M. R.de la Fuente, D. J. B. Jackson, D. O. Lopez, G. R. Luckhurst, M. A. Perez-Jubindo, R. M. Richardson, J. Salud, B. A. Timimi, and H. Zimmermann, Phys. Rev. E **84**, 031704 (2011).
[7] J. V. Selinger, Liq. Cryst. Rev. **6**, 129 (2018).

[8] G. P. Crawford and S. Žumer, Int. J. Mod. Phys. B **09**, 2469 (1995).
[9] S. Meiboom, J. P. Sethna, P. W. Anderson, and W. F. Brinkman, Phys. Rev. Lett. **46**, 1216 (1981).
[10] See Supplemental Material at http://link.aps.org/supplemental/10.1103/PhysRevE.101.032704 for video clips V1.avi and V2.avi and for video clip details and phase-transition related notes.
[11] M. Wojdyr, J. Appl. Crystallogr. **43**, 1126 (2010).
[12] C. Meyer, D. Stoenescu, G. R. Luckhurst, P. Davidson, and I. Dozov, Liq. Cryst. **44**, 232 (2017).
[13] J. W. Park, C. S. Bak, and M. M. Labes, J. Am. Chem. Soc. **97**, 4398 (1975).
[14] M. Press and A. S. Arrott, J. Phys. Colloq. **36**, C1-177 (1975).
[15] M. Conradi, P. Ziherl, A. Šarlah, and I. Muševič, Eur. Phys. J. E. **20**, 231 (2006).
[16] I. I. Smalyukh, R. Pratibha, O. D. Lavrentovich, and N. V. Madhusudana, Liq. Cryst. **30**, 877 (2003).
[17] M. Selmi, J.-C. Loudet, P. V. Dolganov, T. Othman, and P. Cluzeau, Soft Matter **13**, 3649 (2017).
[18] Z. S. Davidson, L. Kang, J. Jeong, T. Still, P. J. Collings, T. C. Lubensky, and A. G. Yodh, Phys. Rev. E **91**, 050501 (2015).
[19] C. N. Kaplan, H. Tu, R. A. Pelcovits, and R. B. Meyer, Phys. Rev. E **82**, 021701 (2010).
[20] B. A. DiDonna and R. D. Kamien, Phys. Rev. Lett. **89**, 215504 (2002).
[21] B. Chakrabarti, Y. Hatwalne, and N. V. Madhusudana, Phys. Rev. Lett. **96**, 157801 (2006).
[22] P. Mach, C. C. Huang, T. Stoebe, E. D. Wedell, T. Nguyen, W. H. de Jeu, F. Guittard, J. Naciri, R. Shashidhar, N. Clark, I. M. Jiang, F. J. Kao, H. Liu, and H. Nohira, Langmuir **14**, 4330 (1998).